



Electrochemical performance of plasma sprayed Cu–Co–SDC mono-layer and Cu–Co–SDC/Cu–YSZ bi-layered anodes manufactured from coarse and fine feedstock powders

Nir Light^a, Olivera Kesler^{b,*}

^a Department of Mechanical Engineering, The University of British Columbia, 2054-6250 Applied Sciences Lane, Vancouver, British Columbia, Canada V6T 1Z4

^b Department of Mechanical and Industrial Engineering, University of Toronto, 5 King's College Road, Toronto, ON, Canada M5S 3G8

HIGHLIGHTS

- ▶ Mono-layer and bi-layer Cu based anodes were manufactured by plasma spraying.
- ▶ Feedstock powder particle size did not have a large effect on anode performance.
- ▶ Anode performance degraded with time due to Cu sintering.
- ▶ Stabilization of the performance after 10–15 h was observed.
- ▶ Bi-layered anode structure only modestly improved the anode polarization resistance.

ARTICLE INFO

Article history:

Received 30 July 2012

Received in revised form

21 September 2012

Accepted 23 September 2012

Available online 9 October 2012

Keywords:

Solid oxide fuel cell

Cu based anode

Plasma spraying

Electrochemical performance

Microstructure

ABSTRACT

Co–Cu–SDC mono-layer and Cu–Co–SDC/Cu–YSZ bi-layered anodes were manufactured by air plasma spraying utilizing coarse and fine feedstock powders. The absolute deposition efficiency was determined for each feedstock material to obtain Cu–Co–SDC coatings with 40 vol% of metallic phases and approximately 5 wt% of Co within the metallic phases. The coatings were characterized for porosity, gas permeability, and phase composition. Electrochemical testing was performed to determine the anode performance and long term stability. Cells with mono-layer anodes manufactured of coarse or fine CuO–CoO–SDC feedstock and Cu–Co–SDC/Cu–YSZ bi-layered anodes were tested at 700 °C and exhibited power densities of 49 mW cm^{−2}, 36 mW cm^{−2}, and 34 mW cm^{−2}, respectively, and polarization resistances of 2.42 Ω cm², 2.23 Ω cm², and 1.98 Ω cm², respectively. Post-test examination revealed that the Cu undergoes sintering and detachment from surrounding particles during testing, resulting in a decrease of triple phase boundary length and performance degradation.

© 2012 Elsevier B.V. All rights reserved.

1. Introduction

Direct oxidation of hydrocarbon (HC) fuels in SOFCs has been investigated extensively recently as an alternative to internal reforming. Anodes for direct oxidation SOFCs are often based on Cu and ceria or doped ceria [1–4]. These anodes demonstrate excellent resistance to carbon deposition, but they exhibit poor performance due to the low catalytic activity of Cu. The addition of materials having a higher catalytic activity, such as Co, to direct oxidation anodes has been investigated to increase anode performance. Cu–Co-based bimetallic anodes have demonstrated

increased performance compared to Cu–ceria anodes and excellent resistance to carbon deposition [5,6].

An additional strategy that has been used to increase anode performance is to optimize anode microstructure by utilizing a bi-layered anode structure. In this approach, the anode is constructed of two distinct layers, a high surface area catalytically active layer near the electrolyte where the electrochemical reaction takes place, and a catalytically inactive conducting layer that collects current and allows the fuel to diffuse to the active layer [7,8].

Bi-layered anodes for direct oxidation of hydrocarbon fuels have been successfully manufactured by wet ceramic processing [e.g. Refs. [9,10]]. In those studies, a YSZ wafer with two porous layers for electrodes separated by a dense layer for the electrolyte was manufactured by tape casting followed by firing. A thin 12 μm anode layer was manufactured by impregnation of nitrate salts into

* Corresponding author. Tel.: +1 416 978 3835; fax: +1 416 978 7753.

E-mail address: kesler@mie.utoronto.ca (O. Kesler).

the YSZ porous wafer followed by firing. The impregnation and firing steps were repeated multiple times to obtain a composition of 40 wt% CeO₂ and 1 wt% Pd. Subsequently, a conductive 100 μ m porous La_{0.7}Sr_{0.3}TiO₃ (LST) layer was deposited on top of the anode layer [9,10].

In a previous study, we have demonstrated the application of atmospheric plasma spray processing to produce Cu–SDC anodes for direct oxidation of hydrocarbon fuels [11]. Plasma spraying has several advantages for the processing of SOFCs, such as short processing time, material compositional flexibility, compatibility with metallic structural supports, and ability to fabricate composite coatings in a single fabrication step, even when the components of the composite have very different melting temperatures. Plasma spraying has been investigated as an alternative manufacturing method to wet ceramic processing for SOFCs [12–14].

In this work, we demonstrate the application of air plasma spray processing to produce bi-layered Cu–Co–SDC anodes, utilizing feedstock powder manufactured of agglomerates of micron-sized particles. This powder morphology has been shown to increase the plasma sprayed anode surface area and performance [15]. Fine CuO, CoO, and SDC feedstock powders were utilized for the processing of anode layers, and coarse CuO and YSZ feedstock powders were used for the processing of anode-side conduction layers. In addition to the bi-layered anode structures, for comparison purposes, we also produced Cu–Co–SDC mono-layer anodes manufactured of coarse and of fine feedstock powders.

2. Experimental procedure

2.1. Material preparation

Commercially available CuO, Co₃O₄, 8 mol% yttria stabilized zirconia (YSZ, (ZrO₂)_{0.92}(Y₂O₃)_{0.08}), and 10 mol% samaria doped ceria (SDC, Ce_{0.8}Sm_{0.2}O_{1.9}) powders (Inframat Advanced Materials, Farmington, CT, U.S.A.) were used to produce the anode layers. Two different SDC powder batches were used in this study: coarse and fine powder batches. Coarse SDC powders were used to produce coarse feedstock Cu–Co–SDC anode layers and fine SDC powders were used to produce fine feedstock Cu–Co–SDC anode layers. The feedstock powders were spherical micron-sized spray dried agglomerates that were flowable for plasma spraying.

To avoid break-up of the powders, the powders were calcined at various temperatures. Particle size analysis of fed powders before and after feeding to the plasma torch was conducted using a wet dispersion laser light scattering particle size analyzer (Mastersizer 2000, Malvern Instruments, Worcestershire, U.K.). The particle size analysis results were used to select the lowest calcination temperature that did not result in break-up of the powders during feeding [16]. When heated above 950 °C, the Co₃O₄ decomposes to CoO. Table 1 shows the powder particle size and the calcination temperatures used for each powder.

SDC powder was sieved to narrower particle size distributions of +32 μ m –45 μ m and –32 μ m utilizing the coarse feedstock and fine feedstock powders, respectively. CuO and CoO powders were

sieved to narrower particle size distributions of +32 μ m –45 μ m and –25 μ m for the coarse and fine feedstock, respectively. The YSZ feedstock powder was sieved to a narrower particle size distribution of +32 μ m –45 μ m. The feedstock powder sieved to a particle size range lower than –32 μ m is referred to here as “fine” feedstock and feedstock powder sieved to a particle size range greater than 32 μ m and lower than 45 μ m is referred to as “coarse” feedstock.

2.2. Plasma spray processing

The atmospheric plasma spray system used for these experiments (Axial III Series 600 DC plasma torch, Northwest Mettech Corp., North Vancouver, Canada) contains a torch in which powder is injected axially between three electrode pairs, and a sample holder rotating at 400 rpm.

Commercially available 2.54 cm diameter porous SS430 disks (media grade (MG) 2, Mott Corporation, Farmington, CT, USA) with a thickness of approximately 1 mm were used as the metallic substrates. A cathode layer was formed by spraying mechanically mixed (La_{0.8}Sr_{0.2})_{0.98}MnO_{3–y} (LSM)–YSZ powders (Inframat Advanced Materials) onto the SS430 substrate using plasma and feedstock conditions developed elsewhere [17]. Fine YSZ powder (Inframat Advanced Materials) suspended in water was used to form the electrolyte on top of the cathode using plasma and feedstock conditions developed elsewhere [14,18]. Table 2 shows the plasma spray process parameters used for production of cathode and electrolyte layers.

Anode layers were formed by spraying mechanically mixed powders utilizing the plasma spray process parameters shown in Table 3. Preliminary screening tests were conducted by air plasma spraying of the feedstock powders onto SS430 porous substrates (media grade (MG) 2, Mott Corporation) and pre-sprayed cathode–electrolyte layers to determine the absolute deposition efficiency of each feedstock material. The absolute deposition efficiency was used to determine feedstock mixing ratios needed to result in the desired anode composition. These coatings were optimized to contain 40 vol% of metallic phases and approximately 5 wt% of Co within the Cu–Co phases. To determine anode gas permeability, 25.4 mm diameter anode layers were sprayed onto SS430 porous substrates. For SEM, porosity characterization, and electrochemical testing, anode layers were sprayed onto the cathode–electrolyte layers. To form a bi-layered anode, an anode

Table 2

Plasma spray process parameter values for production of cathode and electrolyte layers.

Parameter	Values	
	Cathode	Electrolyte
Feedstock	48.2 wt% LSM/51.8 wt% YSZ powder	23.7 wt% YSZ aqueous suspension
Particle size	–45 +32 μ m/ –32 +25 μ m	1.6 μ m (d_{50})
Powder feed rate (g min ^{–1})	40.0	38.1 ^a
Carrier gas flow rate (slpm)	11.7	n/a
Spraying distance (mm)	100	80
Vertical traverse speed (m s ^{–1})	4.25	4.25
No. of vertical passes	60	50
Torch current (A)	549	750
Plasma gas flow rate (slpm)	250	220
Plasma gas composition	76.7% N ₂ /23.3% Ar	80% N ₂ /15% Ar/5% H ₂
Nozzle diameter (mm)	9.5	9.5
Pre-heat temperature (°C)	300	300–350

^a of solids in suspension.

Table 1

Particle sizes of feedstock powders and calcination temperatures.

Powder type	d_{50} (μ m)	Calcining temperature (°C)	Calcining time (h)
CuO (Coarse)	34.5	850	5
Co ₃ O ₄ (Coarse)	38.4	1100	5
YSZ (Coarse)	50.0	1350	5.5
SDC (Coarse)	33.2	1350	5
SDC (Fine)	15.2	1350	5

Table 3
Plasma spray process parameter values for production of mono-layer and bi-layered anodes.

Parameter	Values						
	Screening tests			1" Button cells			
				Mono-layer anode		Bi-layered anode	
	Coarse feedstock CuO–CoO–SDC	Fine feedstock CuO–CoO–SDC	Coarse feedstock CuO–YSZ	Coarse feedstock anode	Fine feedstock anode	Functional layer	Conducting layer
Feedstock (sprayed on SS430 substrate)	40.8 wt% CuO/2.6 wt% CoO/56.6 wt% SDC	29.5 wt% CuO/11.8 wt% CoO/58.8 wt% SDC	40 wt% CuO/60 wt% YSZ	40.8 wt% CuO/2.6 wt% CoO/56.6 wt% SDC	44.1 wt% CuO/2.70 wt% CoO/53.2 wt% SDC	44.1 wt% CuO/2.70 wt% CoO/53.2 wt% SDC	43.2 wt% CuO/56.8 wt% YSZ
Feedstock (sprayed on YSZ electrolyte)	40.8 wt% CuO/2.6 wt% CoO/56.6 wt% SDC	29.5 wt% CuO/11.8 wt% CoO/58.8 wt% SDC	40 wt% CuO/60 wt% YSZ	46.7 wt% CuO/2.92 wt% CoO/50.4 wt% SDC	47.1 wt% CuO/2.75 wt% CoO/50.2 wt% SDC	47.1 wt% CuO/2.75 wt% CoO/50.2 wt% SDC	27.8 wt% CuO/72.2 wt% YSZ
Particle size	–45 +32 μm	–25 μm CuO/–25 μm CoO/–32 μm SDC	–45 +32 μm	–45 +32 μm	–25 μm CuO/–25 μm CoO/–32 μm SDC	–25 μm CuO/–25 μm CoO/–32 μm SDC	–45 +32 μm
Powder feed rate (g min^{-1})	36.1	24.6	43.8	40.8	31.0	31.0	41.7
Carrier gas flow rate (slpm)	15	15	15	15	15	15	15
Feeder drum speed (rpm)	6.0	6.0	0	6.0	6.0	6.0	0
Spraying distance (mm)	100	100	100	100	100	100	100
Vertical traverse speed (m s^{-1})	4.25	4.25	4.25	4.25	4.25	4.25	4.25
Spraying time (s)	50	50	50	50	70	23.2	50.0
Torch current (A)	690	690	690	690	690	690	690
Plasma gas flow rate (slpm)	250	250	250	250	250	250	250
Vol.% nitrogen (balance Ar)	40	40	40	40	40	40	40
Nozzle diameter (mm)	12.7	12.7	12.7	12.7	12.7	12.7	12.7
Pre-heat temperature ($^{\circ}\text{C}$)	300	310	295	300	310	310	310

layer containing CuO, CoO, and SDC fine feedstock powder was deposited initially, followed by deposition of a Cu–YSZ anode conducting layer produced from coarse CuO–YSZ feedstock. These powder mixtures were sprayed through a mask onto the YSZ electrolyte layer to form 11.1 mm diameter anodes. Following the deposition, the coatings were reduced in a N_2 – H_2 mixture (10% H_2) for 3 h.

2.3. Coating characterization

Phase analysis was carried out by X-ray diffraction (XRD, Bruker D8-Discovery diffractometer, Bruker AXS Inc., Fitchburg, WI USA) with Cu K α radiation at 0.01 s^{-1} .

Energy dispersive x-ray spectroscopy (EDX) was performed to determine the volume fraction of Cu and Co present in the anode coatings. Scanning Electron Microscopy (SEM, Hitachi High Technologies America, Pleasanton, CA, USA) imaging of the coatings was performed to observe the porosity and uniformity of the anode microstructures.

Porosity of reduced anodes was determined by statistical image analysis of mounted, sectioned, and polished cross-section SEM micrographs using ImageJ software (National Institutes of Health, USA). To minimize pull-outs that introduce errors in the calculated porosity, coatings were examined by optical microscopy between each polishing step. After the coatings had been polished, ten images were taken for each coating at 0.50 mm intervals along the length of the coating. The images were taken at $3000\times$ magnification with corresponding analysis areas of $42.7 \times 32.0 \mu\text{m}^2$. When an electrolyte layer was present in part of the image, it was omitted with the image analysis software. To clearly distinguish between solid and pore, the contrast was increased and brightness reduced to obtain images predominated by black (pore) and white (solid), utilizing the procedure described elsewhere [19].

Permeability coefficients of reduced anodes were determined using Darcy's law, as described in detail elsewhere [19]. To obtain the thickness required for the permeability coefficient calculation,

fifteen images were taken at equal intervals of 0.5 mm along the coating.

Following the microstructural analysis of anode coatings, single cells were manufactured utilizing coarse feedstock or fine feedstock Cu–Co–SDC anode mono-layers, and fine feedstock Cu–Co–SDC/coarse feedstock Cu–YSZ bi-layered anodes.

2.4. Electrochemical testing

Fuel cell testing was performed using an SOFC test station (AMI, Canada) and a frequency response analyzer (FRA) and potentiostat (Solartron 1260 and 1470E, Solartron Analytical, Farnborough, Hampshire, UK). The test station design includes a thermocouple that measures the temperature close to the cell. Glass felt was utilized to facilitate the sealing. To allow the glass felt to melt and produce a seal, the cells were heated to a maximum temperature of 770°C .

All cells were tested utilizing identical testing profiles. After the glass seal sintering profile was completed, in-situ reduction of the Cu–Co–SDC anodes was conducted in a dry H_2 – N_2 gas mixture (20% H_2) at 700°C at a total flow rate of 200 sccm for 2 h. After reduction, the cells were cooled down to 550°C at a rate of $3^{\circ}\text{C min}^{-1}$ with approximately 50°C decrements and 1 h of dwell time at each temperature. Impedance spectroscopy at open circuit voltage (OCV) conditions and at 0.7 V polarization was conducted at each temperature over the frequency range of 1 mHz–1 MHz, with 50 mV rms voltage perturbation amplitude. Polarization curves were obtained from OCV to 0.3 V. All tests utilized anode and cathode gas flow rates of 200 sccm, with air at the cathode and a humidified (3 vol.% H_2O) 20% H_2 /80% N_2 mixture (on a dry basis) at the anode.

To test the cell performance degradation, the cells were heated to 700°C at a rate of $3^{\circ}\text{C min}^{-1}$ and dwelled for 1 h. Impedance spectroscopy at open circuit conditions and at 0.7 V polarization was then conducted at time intervals of 0.5 h for 26–40 h. In between impedance measurements, cell current was measured at a terminal voltage of 0.7 V.

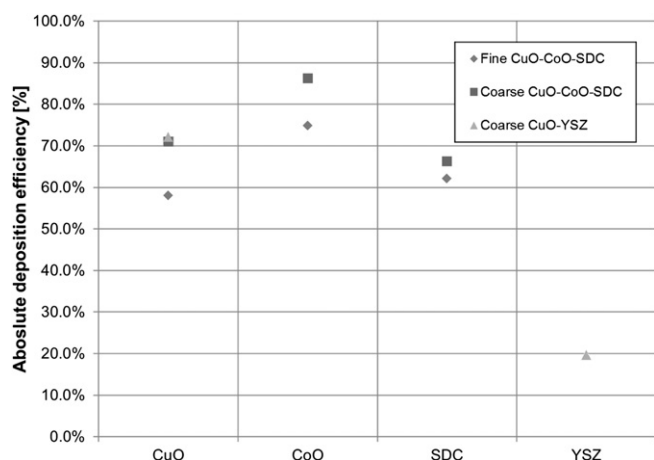


Fig. 1. Absolute deposition efficiencies of the CuO, CoO, SDC and YSZ phases in coatings manufactured using the spraying and feedstock conditions in Table 3.

3. Results and discussion

3.1. Microstructural analysis

3.1.1. Microstructural analysis of screening test coatings

The calculated absolute deposition efficiencies of the CuO, CoO, SDC and YSZ phases sprayed onto pre-deposited cathode and electrolyte layers are shown in Fig. 1. The deposition efficiencies of fine CuO, CoO, and SDC powders are lower than those of coarse CuO, CoO, and SDC powders. The CuO has the largest difference, and the SDC the smallest. This result is expected, due to a higher proportion of evaporation of the fine powder relative to that of the coarse powder. The absolute deposition efficiency of the coarse CuO powder deposited with CoO and SDC is identical to that of CuO powder deposited with YSZ. This result suggests that the absolute deposition efficiency of the CuO is not limited by the extent of melting of the particles, but rather by volatilization of the feedstock at higher plasma powers.

It can also be observed from Fig. 1 that the SDC has a much higher absolute deposition efficiency than that of the YSZ for the conditions utilized. YSZ has a higher melting temperature than SDC (2710 °C for zirconia and 2480 °C for ceria). Moreover, the density of YSZ is lower than that of SDC (5.96 g cm⁻³ for YSZ and 7.22 g cm⁻³ for SDC). It is possible that YSZ experiences a lower residence time in the plasma in comparison to SDC for similarly-sized particles, because similarly-sized particles are lighter and may therefore accelerate to a higher velocity in comparison to those of SDC. These factors may contribute to the lower extent of melting of YSZ compared to the extent of melting of SDC sprayed under identical plasma parameters. The difference could also result from different particle size distributions within the same sieve size fraction.

Table 4
Volume fraction of metallic phases in the coatings and the weight fraction of Co in the Cu–Co phases.

Parameter	Substrate					
	SS430 (Mott MG2) substrate			Suspension electrolyte		
	Coarse feedstock CuO–CoO–SDC (%)	Fine feedstock CuO–CoO–SDC (%)	Coarse feedstock CuO–YSZ (%)	Coarse feedstock CuO–CoO–SDC (%)	Fine feedstock CuO–CoO–SDC (%)	Coarse feedstock CuO–YSZ (%)
Solid volume fraction of metallic phases in coating (vol%)	36.3	39.4	43.1	40.3	35.1	42.8
Co content within metallic phases (wt%)	5.24	5.7	–	6.87	7.46	–

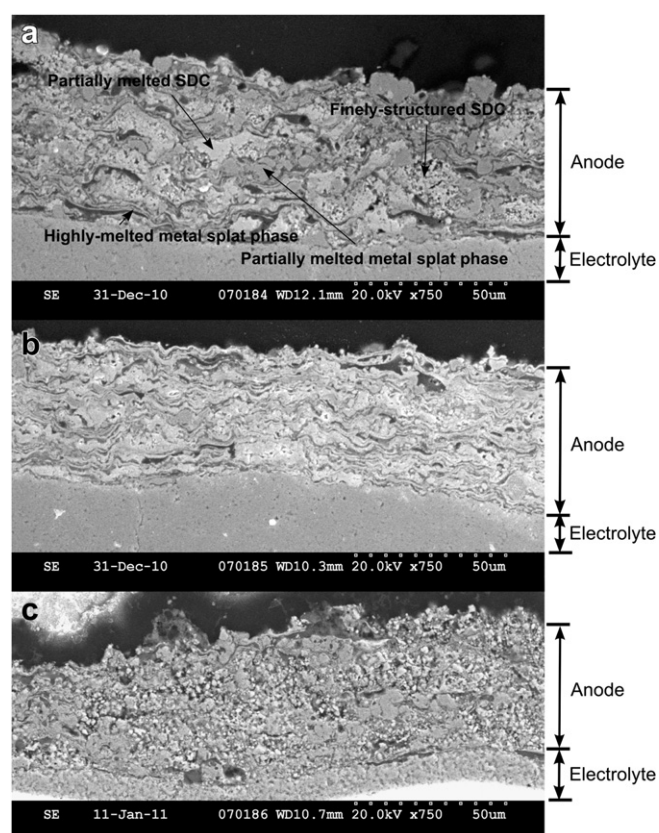


Fig. 2. Cross-section SEM micrographs of (a) coarse Cu–Co–SDC, (b) fine Cu–Co–SDC and (c) coarse Cu–YSZ coatings.

The deposition efficiencies of the CuO, CoO, SDC and YSZ were used to determine the initial feedstock weight ratios required to obtain the target values of 40 vol% of metallic phases in the anode, and 5 wt% of Co within the Cu–Co phases. The resulting mixing ratios of the feedstock powders are shown in Table 3.

3.1.2. Composition analysis of anode coatings

Energy dispersive spectroscopy (EDX) was performed on the coatings after reduction to determine the volume and weight fractions of Cu and Co present in the coatings. The results are shown in Table 4. The volume fractions and weight ratios are close to the targeted values. It can be seen in Table 3 that feedstock mixing ratios are different for the SS430 substrates alone and for YSZ electrolytes on cathodes on the metallic substrates. The differences are due to the dependence of absolute deposition efficiency on the substrate material due to differences in substrate thermal conductivity and surface roughness. Therefore, initial feedstock powder mixing ratios were adjusted corresponding to the substrate used.

Fig. 2 shows SEM cross-section micrographs of (a) a coarse feedstock Cu–Co–SDC layer (b) a fine feedstock Cu–Co–SDC layer, and (c) a coarse feedstock Cu–YSZ coating, all sprayed onto YSZ electrolytes, followed by reduction. The SDC and YSZ phases are the brighter materials in the images of the anode composites. Both in the coarse feedstock Cu–Co–SDC coating and in the fine feedstock Cu–Co–SDC coating, partial melting of the SDC is evident. In the coarse feedstock coating, the SDC partially preserves its finely-structured morphology. This structure is not observed as frequently in the fine feedstock coating. The metallic phases, comprising Cu and Co, were highly melted, but partially melted metallic particles are also evident in the coating. It can be observed that the extent of melting is higher in the fine feedstock coating. In the fine feedstock coating, the splats are thinner compared to the splats of the coarse feedstock coating. This observation is expected due to the use of identical spraying parameters for feedstock powders sieved to different size fractions. Three types of porosity can be observed: Fine pores, resulting from the finely-structured morphology of the SDC particles, oval shaped pores, resulting from the microstructural features of the sprayed particles and gaps between subsequently sprayed particles/splats, and planar porosity, which is observed near metallic particles and can be attributed to a decrease in volume due to reduction of metal oxide to metal.

It can be observed in Fig. 2 that the Cu–Co–SDC coating produced by coarse feedstock powders is less homogeneous than the Cu–Co–SDC coating produced from fine feedstock powder. In the Cu–YSZ coating, shown in Fig. 2(c), it can be observed that the YSZ keeps its finely-structured morphology to a greater extent than the SDC in Fig. 2(a), with both having the same feedstock powder sieve fraction size range of $-45 + 32 \mu\text{m}$. This result is due to the higher extent of melting of SDC in comparison with the YSZ. The lower extent of melting visible from the morphology of the YSZ phase in the coating is consistent with the lower absolute deposition efficiency of YSZ in comparison to that of SDC.

3.1.3. Porosity and permeability analysis of anode coatings

Image analysis was performed on 10 cross-section SEM micrographs each for coarse feedstock Cu–Co–SDC, fine feedstock Cu–Co–SDC, and coarse feedstock Cu–YSZ coatings, using the procedure described in Ref. [19]. Fig. 3 shows the average best estimate porosity value. The error bars indicate the confidence interval with significance level α of 0.05.

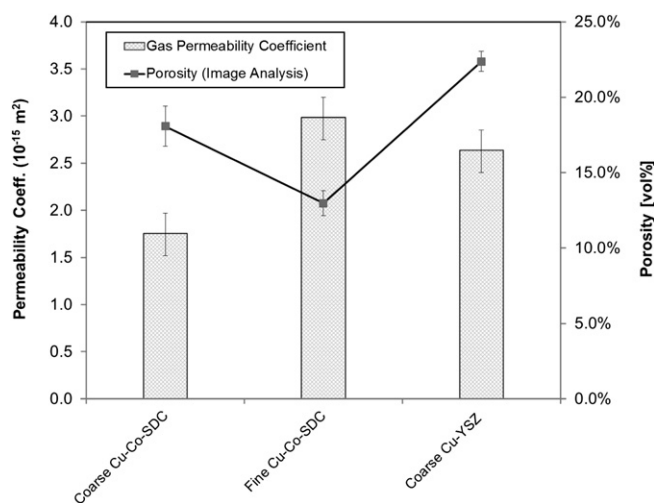


Fig. 3. Porosity and permeability coefficients of reduced anode coatings.

The total porosities of all coatings were in the range of 13.0–22.4 vol%, which is lower than the desired open porosity for SOFC anodes of approximately 30–40 vol%. Both coarse feedstock Cu–Co–SDC and coarse feedstock Cu–YSZ anode layer porosities were higher than those of fine feedstock Cu–Co–SDC anode layers. This result may indicate that partial melting of coarse powders occurred, resulting in increased porosity in comparison to a higher degree of melting of fine feedstock powders, which resulted in decreased porosity. In addition, the Cu–YSZ anode layer porosity was higher than that of coarse feedstock Cu–Co–SDC, which may indicate a lower degree of melting of YSZ particles in comparison to SDC particles. This result is consistent with the absolute deposition efficiencies of these materials.

Permeability coefficients of reduced anode coatings are also shown in Fig. 3. Gas permeability coefficient values are lower relative to those of Ni–YSZ coatings produced in another study utilizing nanostructured NiO–YSZ powders injected radially to a DC plasma torch (F4 torch, Medicoat, Mägenwil, Switzerland) [15]. In our previous work [11] it was demonstrated that the CuO is highly melted even with low energy plasmas. This result is likely at least partially responsible for the low gas permeability coefficient, compared to NiO–YSZ anodes manufactured by plasma spraying.

The gas permeability coefficients do not correlate directly with the porosity values obtained by image analysis. This discrepancy can be explained by noting that open porosity is not the only factor determining the permeability through a porous medium. Gas transport is also affected by the tortuosity factor of the microstructure. In addition, the difference between the open porosity and the total porosity determined by image analysis may not be negligible for low values of total porosity. Image analysis measures the total porosity, including closed porosity. Closed porosity can be created due to geometric shape mismatch between splats. The gas permeability coefficient is dependent on the open porosity, though which the gas can flow. The coarse feedstock coatings have higher porosity values and lower gas permeability values in comparison to the fine feedstock coating. This result may indicate a higher proportion of closed porosity in the coarse feedstock coatings, or a higher tortuosity of the pore space compared to the coatings with lower total porosity. An additional parameter that affects the gas permeability values is the coating thickness. In theory, the gas permeability coefficient should not be affected by the coating thickness, since the coating thickness is considered in its calculation. However, due to the average surface roughness of the substrate, $5.2 \mu\text{m}$ for Mott media grade 2 substrates [14], pinholes in the coating may be present if the coating is not sufficiently thick. Pinholes greatly increase the measured gas permeation, and consequently, the calculated gas permeability coefficient. The average thicknesses of the fine feedstock Cu–Co–SDC, coarse feedstock Cu–Co–SDC, and coarse feedstock Cu–YSZ coatings were 54.1 ± 6.45 , 54.5 ± 4.42 , and $39.9 \pm 3.74 \mu\text{m}$, respectively, at a confidence level of $\alpha = 0.05$. The Cu–YSZ layer is the thinnest of the three types of layers due to the low deposition efficiency. It is possible that pinholes were present in the Cu–YSZ layer as a result of its lower thickness, which made its gas permeability coefficient appear artificially higher than the value corresponding only to the coating microstructure.

3.1.4. Phase analysis of anode layers in full cells

Fig. 4 shows XRD patterns of anode layers produced from CuO, CoO, SDC, and YSZ feedstock powders, before and after reduction with H_2 at 700°C . It can be observed that the crystal structures of the SDC and of the YSZ remained cubic. During spraying, the CuO was partially reduced to Cu_2O . In the case of bi-layered anodes, SDC peaks of the anode layer under the Cu–YSZ conducting layer can be observed. No new phases resulting from inter-reactions

between the two layers are apparent. In the case of fine feedstock and coarse feedstock mono-layer anodes, the Cu_2O , CoO , and CuO were fully reduced to Cu and Co . In the case of bi-layered anodes, no CuO was detected, and a low-intensity peak of Cu_2O can be observed in the reduced coatings at 36.7° . All anodes were reduced under identical conditions. This result demonstrates that one of the layers of the bi-layered anode may have exhibited less open porosity in comparison to the coarse and fine feedstock anode mono-layers, causing less access of the oxides to the reducing H_2 atmosphere.

3.2. Cell testing

3.2.1. Open circuit voltage

The performance of single cells with coarse feedstock Cu-Co-SDC anodes, fine feedstock Cu-Co-SDC anodes, and fine feedstock $\text{Cu-Co-SDC/coarse feedstock Cu-YSZ}$ bi-layered anodes was measured at temperatures between 550°C and 700°C with humidified (3% H_2O) 20% H_2 –80% N_2 mixtures with a total flow rate of 200 sccm at the anode and 200 sccm of air at the cathode. The open circuit voltages (OCV) of the cells were 0.82, 0.89 and 0.87 V for the coarse, fine, and bi-layered anodes, respectively. These OCVs were lower than the OCV predicted by the Nernst equation of 1.05 V. This result can be explained by leakage through the plasma sprayed electrolytes or through the glass seals, or both. When the H_2 concentration at the anode was increased beyond 20%, a rapid decrease of the open circuit voltage was observed for all cells. This result demonstrates the presence of leaks through the electrolyte or glass seals and subsequent combustion. Therefore, all tests were conducted with H_2 – N_2 mixtures at the anode with 20% H_2 on a dry basis.

The open circuit voltage did not degrade substantially in cells with fine feedstock anodes or with bi-layered anodes. However, the coarse anode cell demonstrated substantial degradation of the open circuit voltage over time, with a decrease to 0.74 V after 26 h. Post-testing examination of this cell by SEM revealed that the porosity of the substrate near the cathode was blocked by a layer rich in Cr . This observation can be attributed to rapid chromium oxide formation in the SS430 substrate pores caused by high localized temperatures due to combustion.

3.2.2. Impedance spectroscopy of full cells

Impedance spectroscopy was used to characterize the variation of the cell performance with temperature. Impedance spectra measured near OCV using a four-probe configuration are shown in Fig. 5. In these spectra, the highest frequency real-axis intercept determines the cell series resistance, R_s , and the lowest frequency real-axis intercept determines the total cell resistance, R_t . The width of the impedance arcs on the real axis is the polarization resistance, R_p , which includes the reaction and mass transport resistances of both the anode and cathode.

The resistances of cells with coarse feedstock anode, fine feedstock anode, and bi-layered anode are summarized in Table 5. At 700°C , the cell with the bi-layered anode had the lowest polarization resistance and the cell with the coarse feedstock anode had the highest R_p .

Arrhenius plots of the series and polarization resistance are shown in Fig. 6(a) and (b), respectively. The activation energy of the series resistance R_s is similar to values reported in the literature for APS YSZ electrolytes [20]. The activation energies of the polarization resistances differ to a large extent between the cells, suggesting that different reaction mechanisms dominate the anode performances. The lowest activation energy was observed for the coarse feedstock anodes, suggesting that gas diffusion may be the limiting mechanism for those anodes, since gas diffusion has a weaker temperature dependence than reaction kinetics. This result is consistent with the lower permeability observed for those anodes than for the other two types.

Polarization and power density curves of the full cells at 700°C are shown in Fig. 7. All cells exhibit fairly high activation and ohmic losses, as demonstrated by the low current densities of all cells. In addition, it can be seen that the bi-layered cell is more mass transport limited than the other two types of fuel cell, since its polarization curve demonstrates mass transport limitations at an overpotential of approximately 400 mV, whereas the coarse and fine feedstock anode cells do not demonstrate obvious mass transport limitations as dominant loss mechanisms in the polarization curves to 0.3 V at 700°C . The mass transport limitations observed with 20% H_2 are likely to be more severe than those that would be observed with pure hydrogen fuel at the anode, but the low porosities suggest that mass transport limitations would likely

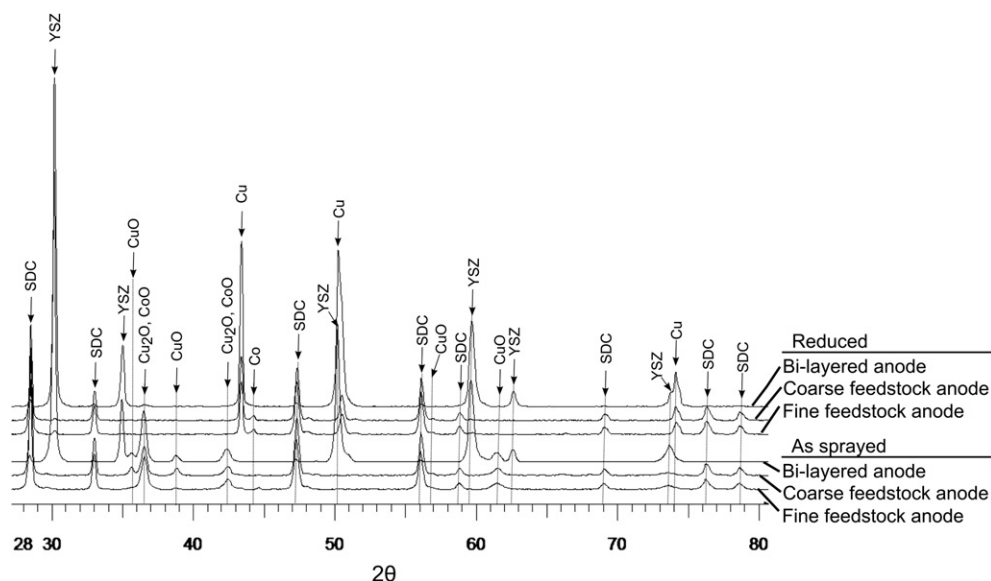


Fig. 4. X-ray diffraction spectra of fine feedstock Cu-Co-SDC , coarse feedstock Cu-Co-SDC , and bi-layered anodes.

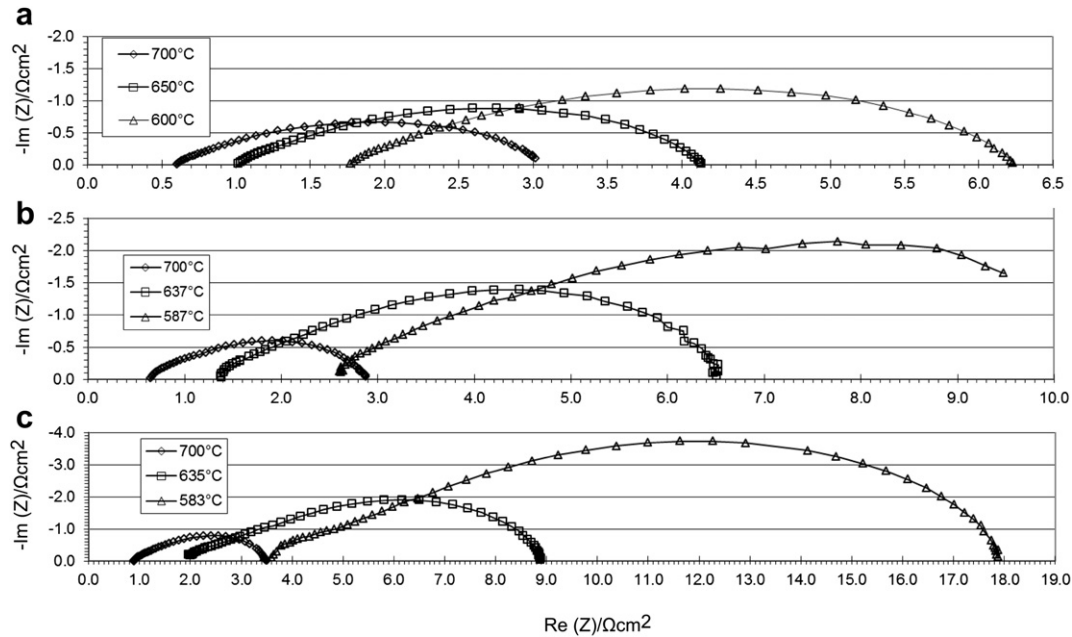


Fig. 5. Impedance spectra of cells with (a) coarse feedstock Cu–Co–SDC anode (b) fine feedstock Cu–Co–SDC anode, and (c) fine feedstock Cu–Co–SDC/coarse feedstock Cu–YSZ bi-layered anode.

also occur in pure hydrogen. Table 6 shows a comparison of the performance of Cu based anodes in this study to Cu based anodes manufactured by wet ceramic methods reported in the literature.

To better understand the extent of mass transport limitations at these operation conditions, impedance spectra of all cells were measured at OCV and at 0.7 V at 700 °C. Fig. 8 shows polarized cell impedance spectra of cells taken at 700 °C 10 h after reduction. It can be seen that the polarization resistances of cells with the coarse feedstock anode and bi-layered anode increase with increased polarization. The higher impedances at increasing polarization are most likely related to diffusion limitations. Gas conversion impedance, in which the concentration of reactant changes through the anode layer, typically occurs with lower peak frequencies and is more readily detectable with a reference electrode in a separate atmosphere from the working electrode [22]. The high frequency impedance does not seem to be affected significantly by the operating voltage. With the fine feedstock cell, the effect of mass transport is not noticeable, demonstrating that the fine feedstock cell is less mass transport limited. In addition, the fine feedstock anode is thicker than both the coarse feedstock anode and bi-layered anode, which provides further evidence that the fine

feedstock anode is the least mass transport limited in its microstructure.

3.2.3. Cell degradation analysis

To study the performance degradation of each cell with time, impedance spectra of the cells were taken at open circuit voltage while the cells dwelled for several hours at 700 °C, as shown in Fig. 9. All spectra demonstrated an increase of both series and polarization resistances, with the polarization resistance increasing at a decreasing rate with time. It can be seen in Fig. 9 that the increase of polarization resistance is associated primarily with the low frequency arc. The high frequency arcs of the spectra remain largely unchanged during the dwell time.

Fig. 10 shows normalized series and polarization resistances of the tested cells over time extracted from the impedance spectra shown in Fig. 9. Both polarization and series resistances of all cells seem to stabilize after the first 10–15 h, with the exception of the fine feedstock mono-layer series resistance.

The degradation reflected by the increase of polarization resistance may be related to several mechanisms. It has been demonstrated by other studies that Cu based anodes operated at 700 °C experience degradation of performance due to sintering of the Cu, resulting in coarsening of the Cu particles and loss of conductivity [23]. This coarsening results in a loss of electronic conductivity, which increases the ohmic resistance if the Cu phase was originally bordering on being not fully percolated, and in a loss of TPB length due to detachment of Cu particles from the ionically conductive phase, i.e. SDC, which increases polarization resistance. To overcome this problem, modifications to the wet ceramic manufacturing process were introduced [3].

To test the hypothesis that degradation occurs due to microstructural changes in the anodes, impedance spectra of the 3 types of cells were taken after several hours of operation at OCV and at 0.7 V, as shown in Fig. 11. Unlike the spectra of the cells with coarse or fine feedstock anodes obtained during the beginning of the test, which did not demonstrate a decrease of the low frequency arc at polarized conditions compared to those at OCV, these spectra of the same cells demonstrated decreased impedance at a polarization of

Table 5
Cell resistances at various temperatures.

Cell	Temperature (°C)	Anode thickness (μm)	R_s (Ωcm ²)	R_t (Ωcm ²)	$R_{p,cell}$ (Ωcm ²)
Coarse feedstock	700	93.4 ± 6.20	0.60	3.02	2.42
Cu–Co–SDC	650		1.01	4.15	3.15
mono-layer	600		1.77	6.27	4.51
Fine feedstock	700	71.25 ± 5.72	0.64	2.87	2.23
Cu–Co–SDC	637		1.38	6.49	5.10
mono-layer	587		2.60	9.80	7.20
Fine feedstock	700	29.9 ± 1.9	0.90	2.87	1.98
Cu–Co–SDC/	637	(functional layer)	1.96	6.49	4.50
coarse	587	39.8 ± 4.8	3.38	17.9	14.5
feedstock		(conductive layer)			
Cu–YSZ					
bi-layered					

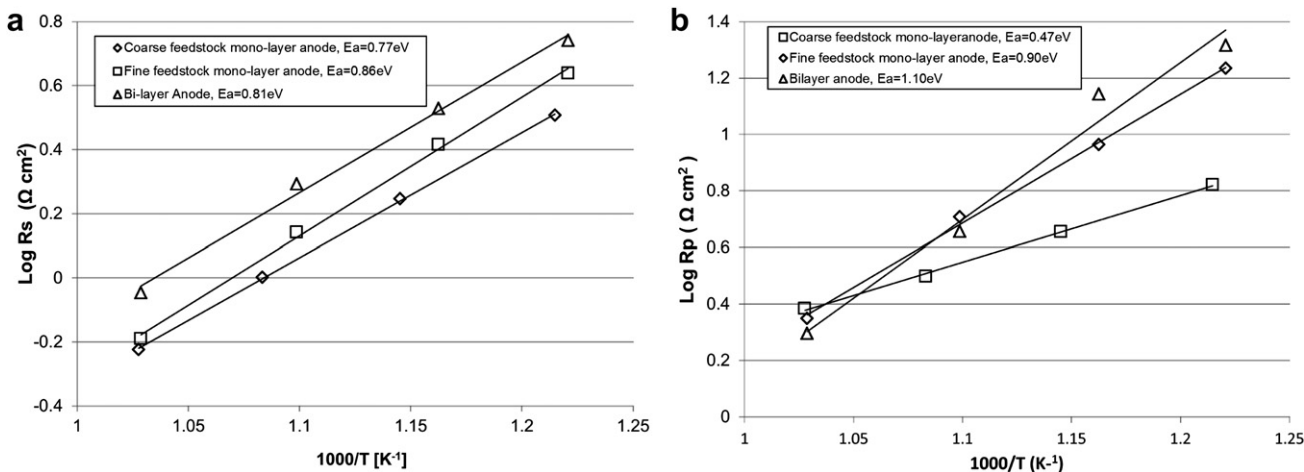


Fig. 6. (a): Arrhenius plot for (a) series resistance (R_s) and (b) polarization resistance of all cells.

0.7 V in comparison to the impedance spectra obtained at OCV. This result demonstrates an improvement of mass transport of those two types of cells, which suggests that a microstructural change may be occurring at the anode. There may also be partial reduction/activation of the cathodes occurring in the cells, which would decrease the R_p of the cells over time.

Unlike the coarse and fine feedstock anode cells, the bi-layered anode cell experienced an increase of the low frequency arc diameter when the cell was polarized. This result can potentially be attributed to the initial low porosity of the Cu–YSZ conducting layer, as determined by image analysis.

3.3. Post-testing examination

3.3.1. Cell microstructure

Cross-section SEM micrographs of a cell with fine feedstock anode after cell testing and a corresponding EDX map are shown in Fig. 12. The microstructure looks more porous in comparison to the reduced fine feedstock anode coating shown in Fig. 2(b). Based on the EDX map, Cu and SDC particles can be identified in the coating. It can be seen in Fig. 12(b) that the indicated Cu particle is detached from the SDC particle above it, and that there is empty volume surrounding the particle. It seems that a Cu particle has undergone

partial sintering, as suggested by the pore volume surrounding the particle. The original fine feedstock coating had splats that appeared to be in close contact with adjacent splats. The coating was less porous, and no isolated particles were observed having surrounding pore volume. The splats in the anode after testing are still attached to the surrounding particles, but with less material connecting them. This result indicates that the Cu particles may have partially detached from the surrounding particles during testing due to sintering.

Microstructural degradation of cermet anodes in SOFCs is often attributed to Ostwald ripening [24]. This mechanism might be assisted by a release of residual stresses that result from the PS processing. As the splats hit the substrate and rapidly cool and solidify, they are constrained mechanically by the underlying splats as their volume contracts due to the cooling. This constraint results in tensile residual stress, as reported in other studies [25]. The residual stress causes a tendency of the CuO or Cu particles to contract during long operating times at elevated temperatures. Since the melting temperature of Cu is lower than that of CuO, once the cells have been heated and the CuO has been reduced to Cu, the Cu will be closer to its melting temperature than CuO, allowing higher mobility of the Cu phase compared to the CuO formed

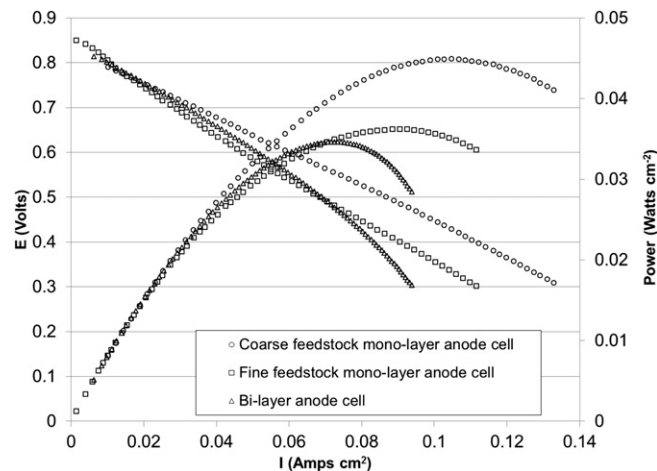


Fig. 7. Polarization curves of cells with coarse feedstock mono-layer anode, fine feedstock mono-layer anode, and bi-layered anode at 700 °C.

Table 6
Performance of Cu based anodes manufactured by wet ceramic methods appearing in the literature.

Cell composition	Power density at 0.7 V (mW cm ⁻²)	Ref.
Anode: Ni0.5Cu0.5–CGO (Ce0.8Gd0.2O1.9) Cathode: 30 wt% CGO/44 wt% LSM/24 wt% pore former	86 (extrapolated for 700 °C)	[1]
Anode: nano-composite Cu–GDC–YSZ adhered to core YSZ particles (30 vol% CuO/30 vol% GDC/10 vol% YSZ – 30 vol% YSZ), 40 vol% porosity Cathode: 50 wt% LSM/50 wt% GDC	90 (tested at 800 °C)	[2]
Anode: 16 vol% Cu and 12 vol% CeO ₂ , 65 vol% porosity Cathode: 50 wt% YSZ/50 wt% LSM	236 (tested at 700 °C)	[3]
Anode: 40 wt% Cu and 60 wt% CeO ₂ , screen printed on YSZ electrolyte substrate and calcined Cathode: LSM cathode paste, screen printed on YSZ electrolyte and calcined	58 (tested at 750 °C)	[21]

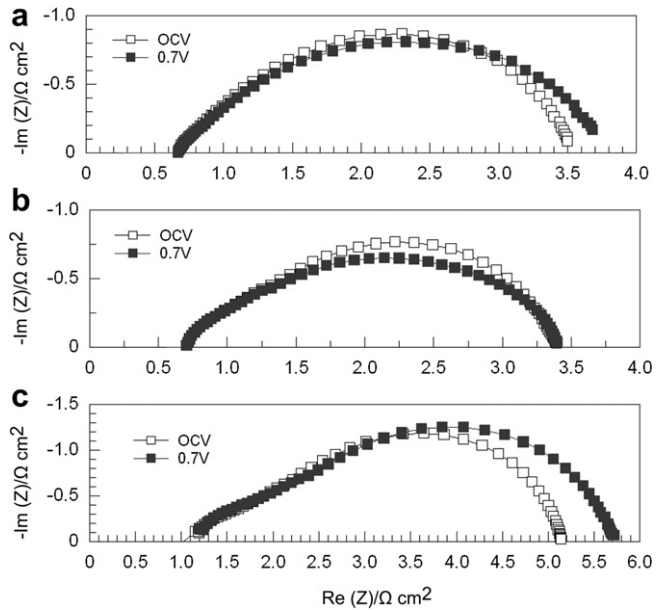


Fig. 8. Impedance spectra of cells with (a) coarse feedstock anode (b) fine feedstock anode and (c) bi-layered anode at OCV and at 0.7 V polarizations at 700 °C.

during coating deposition. Then, the residual stresses may cause the Cu to detach from the surrounding particles.

Cross-section SEM micrographs of a tested cell with a coarse feedstock anode are shown in Fig. 13. The non-conductive SDC looks brighter in SEM and the conductive Cu looks darker. It can be observed that a large number of the Cu particles have porosity surrounding them, and they are disconnected from the matrix in the plane of the micrograph, which was not observed in micrographs of

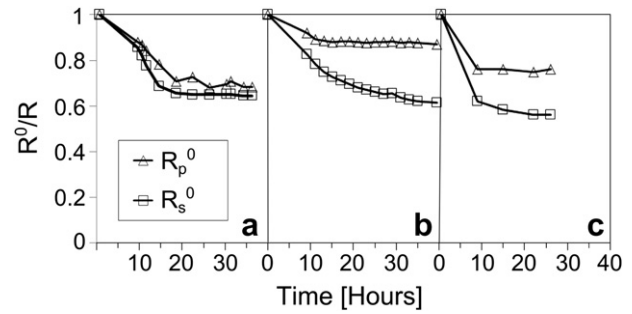


Fig. 10. Normalized series and polarization resistances over time of (a) cell with coarse feedstock anode, (b) cell with fine feedstock anode, and (c) bi-layered anode cell dwelled at 700 °C for several hours.

the coating prior to testing. The dark areas are either pores or pores filled with epoxy resin. It seems that the Cu particles undergo sintering and detach at least partially from the surrounding particles, resulting in some empty volume surrounding the Cu particles, and a less-connected conductive network of Cu compared to the anodes prior to cell testing.

An SEM micrograph of a polished cross-section of a tested cell with a bi-layered anode is shown in Fig. 14. Unlike the other anodes, which demonstrated coarsening of the microstructure and high porosity, it seems that the Cu in the anode layer is highly sintered, resulting in reduced porosity. The conduction layer has a morphology with a fine pore structure due to the low extent of melting of the YSZ during fabrication. This observation agrees with the observed low absolute deposition efficiency of YSZ. One possible reason for the lack of increased porosity due to coarsening of the microstructure observed in the bi-layered anode cells, in contrast with the observations of the cells with fine and coarse feedstock mono-layer anodes, is a possible stabilizing effect of the conductive

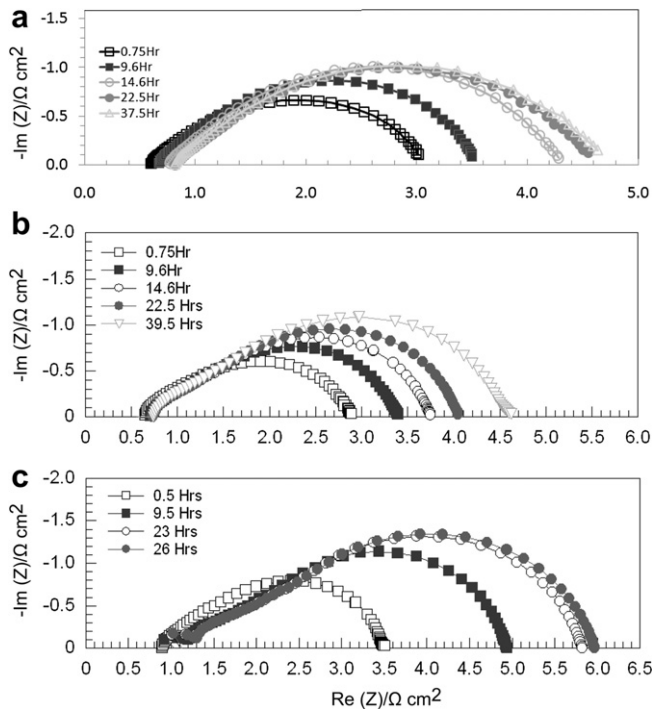


Fig. 9. Impedance spectra at OCV for cells with (a) coarse feedstock anode mono-layers (b) fine feedstock anode mono-layers, and (c) bi-layered anodes dwelled at 700 °C for different dwell times after reduction.

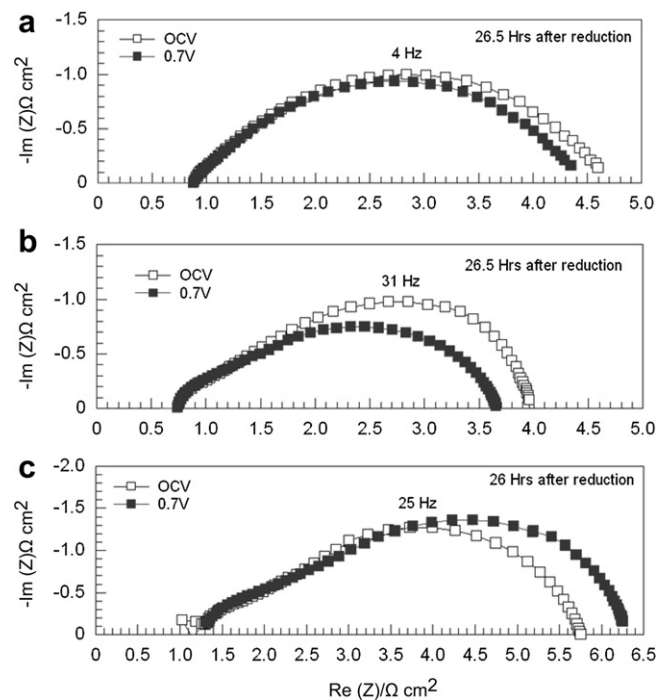


Fig. 11. Impedance spectra of cells with (a) coarse feedstock anode (b) fine feedstock anode and (c) bi-layered anode at OCV and at 0.7 V obtained after 26 and 26.5 h of operation.

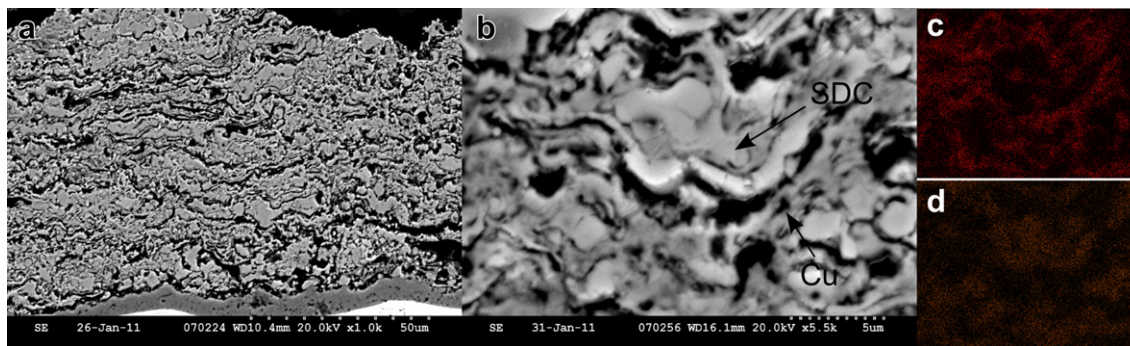


Fig. 12. SEM micrograph with magnification of (a) 1000 \times and (b) 5500 \times and high magnification (5500 \times) EDX maps of (c) Cu and (d) Ce of polished cross-section of fine feedstock anode tested for 40 h.

layer, which makes the Cu less volatile, or due to a lower initial porosity, which leads to more densification during sintering at extended times at the operating temperature.

3.3.2. Local delamination

Fig. 15 shows an SEM micrograph of a polished cross-section of a cell with a fine feedstock anode. Delamination of the anode is present locally, at a point at which the electrolyte has an irregular 'bump' in its shape. This delamination can occur when the anode is constrained mechanically while thermally expanding, thus creating localized stresses parallel to the anode–electrolyte interface that may cause delamination in areas of the anode where its geometry is not planar, but curved such as around a bump, due to the presence of localized stress concentrations. Such local delamination contributes to the overall degradation of performance, since a portion of the anode becomes inactive for electrochemical reaction [26]. One possible cause for anode delamination is the heating rates of 5 $^{\circ}\text{C min}^{-1}$ required to form the glass seal. Due to the difference between the thermal expansion coefficients (CTEs) of YSZ ($10.5\text{--}11.0 \times 10^{-6} \text{ K}^{-1}$) and of Cu ($16.5 \times 10^{-6} \text{ K}^{-1}$), heating to the operating temperature may cause anode delamination due to the resulting thermal expansion mismatch. At this point, it is not clear whether the observed local delamination is an outcome of the heating cycle during the test or was present after fabrication and prior to testing. No delaminations were observed by SEM in the as-sprayed cells, but they may have been present in regions of the cells that were not in the image planes.

3.3.3. Substrate oxidation

SEM examination of the SS430 porous substrate of the coarse cell after the test demonstrated a loss of porosity, with Cr detected

by EDX inside the substrate pores. This result may have been caused by a local increase of temperature of the SS430 substrate resulting from combustion of gases leaking across the cell or its seals, leading to the rapid formation of a Cr_2O_3 layer on the stainless steel support. SEM micrographs on additional cross-sections of the same cell did not show the same loss of porosity due to the formation of a chromia layer. This result indicates that the combustion occurred locally, likely resulting from gas leakage either through the electrolyte, through the seal, or through delaminated regions between cell layers. The formation of thick localized chromia layers and their hypothesized origin due to leakage-induced combustion are in agreement with the lower open circuit voltage observed with this cell. Fig. 16 shows SEM micrographs of two polished cross-sections of a cell with a coarse feedstock anode, one with visibly blocked substrate porosity, and one from a different location in the same cell without any visibly blocked substrate porosity.

3.3.4. Outlook

The present performances of the Cu based anodes manufactured by plasma spraying in this study are fairly low in comparison to Cu based anodes manufactured by wet ceramic processing, as shown in Table 6. There are several factors that decrease the cell performance that can be further optimized. Firstly, the mass transport properties of the plasma sprayed Cu based anodes are a factor in the current low performance of these cells. Mass transport can be improved by utilizing pore former, which is an organic material that is added to the feedstock powder and burned out after the anode has been deposited to increase the porosity of the anode. The application of pore former is used as a standard procedure to control the porosity of SOFC electrodes manufactured by wet ceramic processing. The addition of pore former to the feedstock

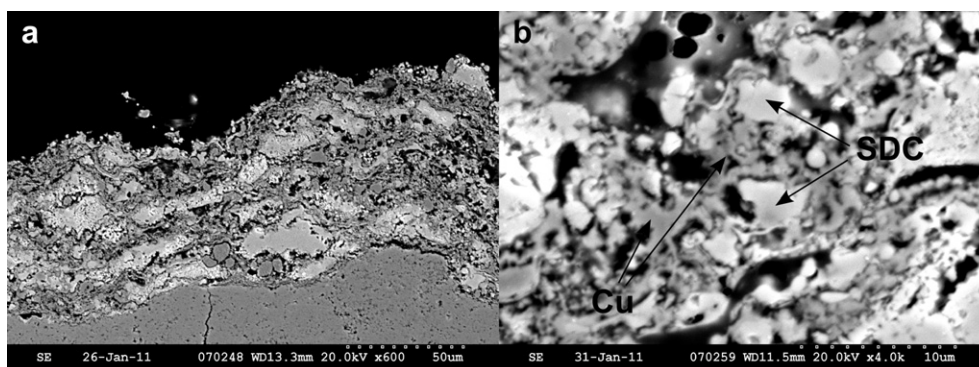


Fig. 13. SEM micrographs with magnification of (a) 600 \times and (b) 4000 \times of a polished cross-section of a coarse feedstock anode tested for 40 h.

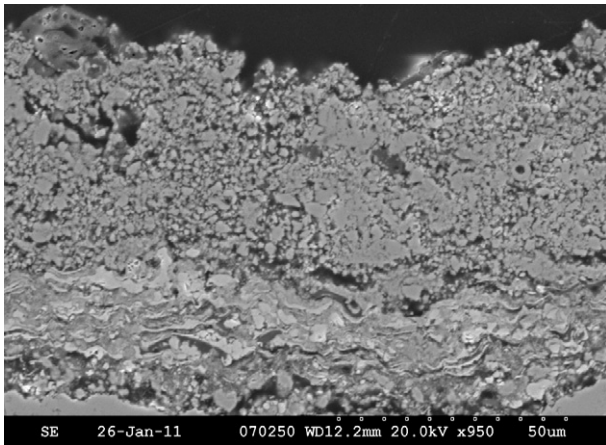


Fig. 14. SEM micrograph of a polished cross-section of a bi-layered anode tested for 40 h.

materials has also been applied recently in manufacturing of SOFC anodes by plasma spraying. Recent studies on Ni–YSZ utilizing an identical plasma spraying system demonstrated that the application of pore former resulted in a five-fold increase of the gas permeability of these anodes [27].

An additional strategy to improve mass transport in Cu–Co anodes is to apply a higher content of Co, which has a higher melting temperature than that of Cu. This can improve the porosity of the anode due to a lower degree of melting of the CoO feedstock during the plasma spraying process. In addition, a higher Co content can improve the thermal stability of Cu based anodes, as has been demonstrated in Cu–Co-based anodes manufactured by wet ceramic processing [6]. Since Cu has an important role in Cu–Co-based anodes to suppress carbon deposition, a too-high Co content might cause significant carbon deposition and therefore might not be practical in direct oxidation anodes. Therefore, further optimization is required to determine the optimal Co content to improve the mass transport and thermal stability of plasma sprayed Cu–Co-based anodes without causing significant carbon deposition when HC fuels are used.

The performance of plasma sprayed Cu–Co-based anodes can further be improved by increasing the active surface area of the anode. One strategy to increase the anode surface area applied recently in plasma spraying of SOFC electrodes is using sub-

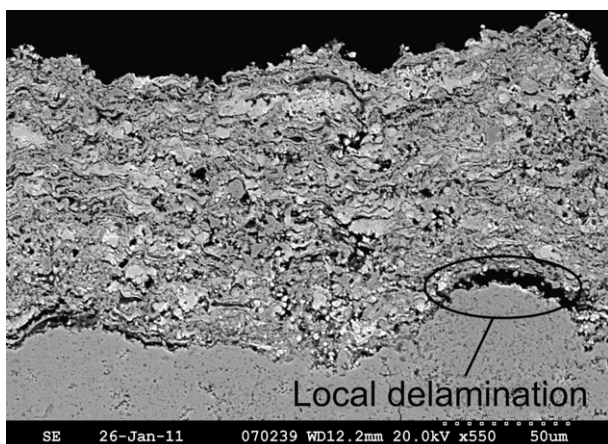


Fig. 15. SEM micrograph of polished cross-section of a cell with a fine feedstock anode showing localized delamination.

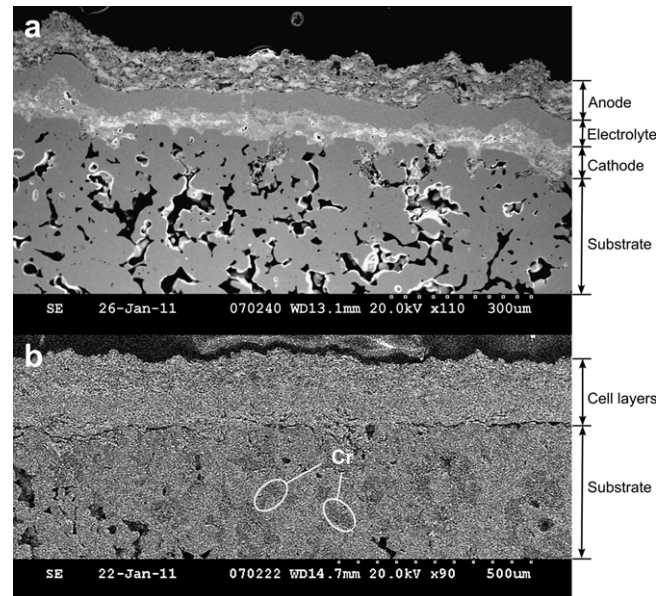


Fig. 16. Cross-section micrographs of a cell with a coarse feedstock anode demonstrating (a) open porosity in the substrate, and (b) blocked porosity in the substrate at a different location.

micron feedstock particles suspended in a liquid, in suspension plasma spraying (SPS) [28]. SPS seems to be a promising technology to increase the performance of plasma sprayed SOFCs.

The other cell layers, namely the cathode and electrolyte, also need to be further improved to increase the performance of SOFCs with plasma sprayed Cu based anodes. The low electrolyte gas tightness decreased the OCV obtained in cells tested in this current study. Better gas tightness will increase the OCV, and therefore improve cell performance. In addition, better gas tightness will allow the application of pure H_2 as a fuel, which would improve cell performance as well, due to the effect of anode gas composition on mass transport and the limiting current density. The cathode materials and microstructure need to be further optimized to improve the cell performance. The cathode microstructure can be improved by applying a bi-layered structure with a finely-structured active layer that can be manufactured by SPS and a cathode support layer whose porosity can be improved by utilizing pore former added to the feedstock powder. The application of cathode materials that are more suitable than LSM–YSZ for operation at intermediate temperature range, such as $La_{0.6}Sr_{0.4}Co_{0.2}Fe_{0.8}O_{3-\delta}$ (LSCF) can improve cell performance as well.

4. Conclusions

Cu based mono-layer and bi-layered anodes were fabricated by air plasma spraying of coarse and fine feedstock powders. Cells were tested with 20% H_2 /80% N_2 anode gas mixtures humidified with 3% H_2O . Cells with coarse feedstock, fine feedstock and bi-layered anodes tested at 700 °C exhibited power densities of 24 $mW\ cm^{-2}$, 20 $mW\ cm^{-2}$, and 22 $mW\ cm^{-2}$ at 0.7 V, and polarization resistances of 2.42 $\Omega\ cm^2$, 2.23 $\Omega\ cm^2$, and 1.98 $\Omega\ cm^2$, respectively. Performances of all of the cells degraded with time. However, stabilization of the performance after 10–15 h was observed for most of the cells. Cells undergo microstructural changes and possible sintering of Cu during extended operating times. Localized anode delamination was also observed after cell testing. Overall, it was found that the use of the bi-layered structure only modestly improved the anode polarization resistance

compared to single-layer cells. Improvements in the mass transport properties of the layers are needed in order to further improve the performance of the cells.

Acknowledgments

The authors gratefully acknowledge financial support from the Natural Sciences and Engineering Research Council (NSERC) of Canada and Northwest Mettech Corporation, as well as from the Solid Oxide Fuel Cells Canada Strategic Research Network sponsored by NSERC and other sponsors listed at www.sofccanada.com, and the National Research Council Institute for Fuel Cell Innovation (NRC-IFCI) for access to their facilities. The authors gratefully acknowledge the assistance of Dr. Dave Waldbillig with spraying of suspension electrolytes, and the support of Mr. Jason Fahlman of NRC-IFCI during the electrochemical testing.

References

- [1] G. Chen, G. Guan, Y. Kasai, H.-X. You, A. Abudula, J. Solid State Electrochem. 16 (2012) 2071–2077.
- [2] J.-J. Lee, E.-W. Park, S.-H. Hyun, Fuel Cells 10 (2010) 145–155.
- [3] S. Jung, C. Lu, H. He, K. Ahn, R.J. Gorte, J.M. Vohs, J. Power Sources 154 (2006) 42–50.
- [4] M.D. Gross, J.M. Vohs, R.J. Gorte, J. Mater. Chem. 17 (2007) 3071–3077.
- [5] S.W. Jung, J.M. Vohs, R.J. Gorte, J. Electrochem. Soc. 154 (2007) B1270–B1275.
- [6] M.D. Gross, J.M. Vohs, R.J. Gorte, Electrochim. Acta 52 (2007) 1951–1957.
- [7] F. Zhao, A.V. Virkar, J. Power Sources 141 (2005) 79–95.
- [8] V. Vashook, J. Zosel, R. Muller, P. Shuk, L. Vasylechko, H. Ullmann, U. Guth, Fuel Cells 6 (2006) 293–302.
- [9] M.D. Gross, J.M. Vohs, R.J. Gorte, Electrochem. Solid State Lett. 10 (2007) B65–B69.
- [10] M. Gross, R. Gorte, J. Vohs, in: K. Eguchi, J. Mizusaki, S. Singhal, H. Yokokawa (Eds.), 10th International Symposium on Solid Oxide Fuel Cells (SOFC-X) 7 2007, pp. 1349–1354.
- [11] Nir Benoved, O. Kesler, J. Power Sources 193 (2009) 454–461.
- [12] R. Hui, Z. Wang, O. Kesler, L. Rose, J. Jankovic, S. Yick, R. Maric, D. Ghosh, J. Power Sources 170 (2007) 308–323.
- [13] R. Henne, J. Therm. Spray Technol. 16 (2007) 381–403.
- [14] D. Waldbillig, O. Kesler, J. Power Sources 191 (2009) 320–329.
- [15] A. Ansar, D. Soysal, G. Schiller, Int. J. Energy Res. 33 (2009) 1191–1202.
- [16] N. Light, Ph.D. Dissertation, University of British Columbia, 2012, pp. 72–74.
- [17] B.D. White, O. Kesler, Lars Rose, J. Power Sources 178 (2008) 334–343.
- [18] D. Waldbillig, O. Kesler, Surf. Coat. Technol. 203 (2009) 2098–2101.
- [19] N. Light, O. Kesler, J. Power Sources, *in press*.
- [20] Z. Li, G. Zhang, X.-J. Ning, C.-X. Li, H. Liao, C. Coddet, Mater. Sci. Eng. B 137 (2007) 24–30.
- [21] A. Fuerte, R.X. Valenzuela, M.J. Escudero, L. Daza, ECS Trans. 25 (2009) 2173–2182.
- [22] S. Primdahl, M. Mogensen, J. Electrochem. Soc. 145 (1998) 2431–2438.
- [23] C. Lu, W.L. Worrell, in: Meeting Abstracts, 2004 Joint International Meeting – 206th Meeting of the Electrochemical Society/2004 Fall Meeting of the Electrochemical Society of Japan, MA 2004-02, 2004, pp. 1723.
- [24] L. Holzer, B. Iwanschitz, Th. Hocker, B. Münch, M. Prestat, D. Wiedenmann, U. Vogt, P. Holtappels, J. Sfeir, A. Mai, Th. Graule, J. Power Sources 196 (2011) 1279–1294.
- [25] S. Kuroda, T. Fukushima, S. Kitahara, J. Therm. Spray Technol. 1 (1992) 325–332.
- [26] J.I. Gazzarri, O. Kesler, J. Power Sources 167 (2007) 430–441.
- [27] Michael Poon, Olivera Kesler, J. Power Sources 210 (2012) 204–217.
- [28] O. Marchand, E. Saoutieff, P. Bertrand, M.-P. Planche, O. Tingaud, G. Bertrand, Surf. Coat. Technol. 205 (2010) 993–998.